Heliyon 10 (2024) e31837

Contents lists available at ScienceDirect

Heliyon

journal homepage: www.cell.com/heliyon

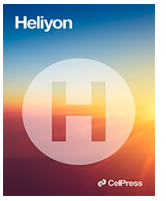

Research article

Nanoquantification of RUNX2 by a 1,1′-carbonyldiimidazole-diamond mediated sandwich assay for osteogenic differentiation

Qingshan Sun [a,1], Wei Zhu [b,1], Endong Shi [a], Maheng Bai [c], ZengJiang Liu [c], Zhiquan Yang [c,*]

[a] Department of Bone Surgery, The Third Hospital of Shandong Province, Jinan, Shandong, 250031, China
[b] Department of Orthopaedics, Changshu Zhitang People's Hospital, Changshu, Jiangsu, 215531, China
[c] Department of Second Orthopedics (Department of Joint Surgery), The Xingyuan Hospital of Yulin (The fourth of Yulin Hospital), Yulin, Shaanxi, 719000, China

ARTICLE INFO

Keywords:
Runt-related transcription factor
Nanodiamond
Sandwich pattern
Antibody orientation

ABSTRACT

Adipose tissue-derived stem cells (ADSCs) possess the capability to modulate the immune response and alleviate inflammation, rendering them a promising therapeutic option for various conditions, including autoimmune diseases, cardiovascular diseases, and tissue injuries. The osteogenic differentiation in ADSCs plays a pivotal role in fracture healing, bone growth, and the overall bone turnover process, governed by intricate interactions. Runt-related Transcription Factor 2 (RUNX2) is a key player in mineralized tissue generation and is typically found in the early stages of osteogenic differentiation. The objective of this study was to develop a high-affinity sandwich biosensor for the quantification of RUNX2. 1,1′-Carbonyldiimidazole-modified nanodiamond was immobilized on an amine-modified interdigitated electrode surface, followed by the use of a capture antibody to facilitate antigen interaction. A sandwich assay was conducted with the antibody, and the limit of detection for RUNX2 was calculated as 0.1 ng/mL, with a regression value (R^2) of 0.9914 over a linear range of 1–2000 ng/mL. Furthermore, biofouling experiments with a nonimmune antibody, BSA, and TNF-α did not yield any current responses, indicating the specific detection of RUNX2. Additionally, RUNX2-spiked serum exhibited an increasing current response at all concentrations, confirming the selective detection of RUNX2.

1. Introduction

Bone is a complex tissue involved in various physiological processes, such as mineral storage, body movement, endocrine function, and hematopoiesis [1,2]. Bone fractures are common and represent a significant level of trauma leading to the loss or fracture of bone tissue [2]. Generally, bone tissues possess the capacity for regeneration and self-repair through the recruitment of surrounding osteoprogenitor cells [3,4]. However, in cases of severe damage, the healing process may be delayed, resulting in scar formation [5].

* Corresponding author.
E-mail address: yzq13689224943@sina.com (Z. Yang).
[1] Equally contributed.

https://doi.org/10.1016/j.heliyon.2024.e31837
Received 4 December 2023; Received in revised form 29 March 2024; Accepted 22 May 2024
Available online 23 May 2024

Bone tissue engineering has emerged as a well-established technique, facilitating the creation of biocompatible bone substitutes with substantial potential for bone regeneration [6]. Researchers have utilized various nanomaterials, such as hyaluronic acid and gelatin encapsulated with silica nanoparticles loaded with metformin, which has proven effective in neutralizing cellular aging and has been applied in various tissue engineering applications [7,8]. Recently, adipose tissue-derived stem cells (ADSCs) have been isolated and employed for various therapeutic purposes, playing a significant role in bone tissue engineering. ADSCs offer several advantages, including easy isolation from adipose tissue, high yield, and low morbidity. They are also more accessible and less invasive to obtain compared to other mesenchymal stem cell (MSC) sources, such as bone marrow. ADSCs contribute to the treatment of conditions associated with cardiovascular diseases, autoimmune diseases, and tissue injuries [9]. These features of ADSCs are gaining more attention in the development of tissue engineering and medicine for bone regeneration.

Developing strategies to enhance the osteogenic differentiation of ADSCs holds promise for advancing bone regeneration and treatment. Numerous studies have sought to improve the osteogenic differentiation process, often employing the use of ascorbic acid and dexamethasone in various experimental approaches, such as tissue engineering. Monitoring the differentiation of stem cells is crucial for identifying conditions that enhance the differentiation process. Osteogenic differentiation in ADSCs is commonly assessed by monitoring alkaline phosphatase activity, cell number, and calcium deposition. Transcription factors such as ZNF25, SOX9, RUNX2, and osterix also play a significant role in monitoring osteogenic differentiation. RUNX2, a transcription factor belonging to the RUNX family, containing the DNA binding domain RUNT, is particularly essential in osteogenic differentiation. Specifically, runt-related transcription Factor 2 (RUNX2) plays a major role in tissue mineralization and is typically present in the early stages of osteogenic differentiation [10]. This process involves the transformation of mesenchymal stem cells (MSCs) into osteoblasts, the cells responsible for bone formation. MSCs are multipotent cells with the ability to differentiate into various cell types, including osteoblasts. RUNX2 acts as a crucial regulator determining MSC commitment to the osteogenic lineage. Moreover, it has been demonstrated that the activity of runt-related transcription Factor 2 (RUNX2) regulates MLP1 and TAZ, stimulating the expression of RUNX2 [11]. Quantifying the level of RUNX2 is crucial for monitoring osteogenic differentiation. This research aims to develop a sandwich dielectric biosensor to quantify the level of RUNX2 for measuring osteogenic differentiation in ADSCs.

Various biomarkers play a crucial role in diverse medical applications, including diagnosis, drug delivery, and therapeutics [12–20]. Biosensors, utilizing biological molecules or organisms, are employed to detect the presence of specific substances in biological fluids, facilitating the identification of biomarkers for disease diagnosis [21,22]. These devices consist of a biomolecule recognition element, such as an enzyme, antibody, or DNA sequence, and a transducer that converts the biomolecular interaction signal into a measurable optical, electrical, or mechanical signal. Biosensors have wide-ranging applications in medicine, environmental monitoring, and food safety. In the medical field, they can detect disease biomarkers or monitor drug levels in the blood. Enhancing biosensor performance is essential for detecting target molecules at lower levels, enabling early disease diagnosis. The advent of nanotechnology has led to the synthesis of various nanomaterials with different shapes and sizes, proving highly effective for biomedical applications [6,23]. Commonly used materials include graphene, silica, magnetic materials, gold, silver, and quantum dots, synthesized in forms such as nanoparticles, nanostars, nanotubes, nanourchin, nanoflower, and nanorod. These nanomaterials offer a higher surface area and increased stability in biological fluids, making them promise for various biomedical applications, including drug delivery and biosensors [24–26]. Nanomaterial-conjugated biomolecules demonstrate stronger binding on the sensor electrode surface, enhancing analyte-target interactions and lowering the limit of detection. Among various materials, diamond stands out as an established choice for surface functionalization due to its excellent chemical and electronic properties [27]. Carbon-derived materials, specifically graphene, carbon nanowires, carbon nanotubes, and carbon nanourchins, have established themselves in medical diagnosis, particularly in biosensing and bioimaging applications. These materials exhibit remarkable electrochemical properties and electron transfer capabilities, making them well-suited for electrochemical biosensor technologies. Diamond, as a unique carbon material composed of sp3 carbon, holds great promise for futuristic applications in therapeutics and biosensing. It offers excellent biocompatibility, ease of bioconjugation, cost-effectiveness, chemical inertness, noncytotoxicity, and impressive fluorescent capacities, along with distinctive optical properties. Nanodiamonds, in particular, have been identified as suitable substrates for monitoring cellular activities, tracking stress regions, maintaining fluorescence for in vivo molecular imaging, and modulating the immunity and tension of the target molecule. Moreover, nanodiamond proves to be an excellent material for controlling biomolecular attachment on sensor surfaces, a critical aspect for minimizing the signal-to-noise ratio. Research has also shown that nanocrystalline diamond exhibits exceptional long-term bonding stability with DNA, enhancing DNA hybridization without degradation [28]. Furthermore, diamond serves as an excellent transducer material for biosensing, particularly in electrochemical sensors [29]. In this study, nanodiamond was affixed to the sensing electrode surface, and subsequently, a RUNX2-specific antibody was immobilized on the nanodiamond using 1,1′-Carbonyldiimidazole (CDI) and (3-aminopropyl) triethoxysilane (APTES) chemical linkers. A sandwich assay with two different antibodies against a single target (RUNX2) was conducted on the sensing surface for quantification. The primary objective of this study was to provide quantification of RUNX2 through the sandwich assay, and this high-performance analysis is expected to establish a fundamental platform for determining osteogenic differentiation in ADSCs. Furthermore, it has the potential to serve as an alternative to other detection systems/strategies for assessing biomarkers associated with osteogenic differentiation.

2. Materials and methods

2.1. Materials

CDI, Potassium chloride, RUNX2, BSA, TNF-α, RUNX2 mouse monoclonal and rabbit polyclonal antibodies, phosphate buffered saline (PBS) with pH 7.4, APTES and nanodiamond were purchased from Sigma Aldrich, USA. Human serum was received from

Fitzgerald Industries International, USA. Silicon wafer (300 mm; N-type without dopant) was from Fitronics, Malaysia. 10 nm-sized nanodiamond octadecane functionalized was from Sigma Aldrich, USA. Thermal evaporator was from ZHD300 Thermal Evaporator, BEIJING TECHNOL SCIENCE CO. LTD. (China). UV-lamp and high-Performance Ce Certified Compact Spin Coater for Wafer were obtained from Made-in-China (China). Non-immune antibody was from the pre-immune serum. A picoammeter (Keithley, Tektronix, USA) was used to supply the power at 0–2 V with an interval of 0.1 V using a dual probing needle. Measurements were done at room temperature by maintaining the wet-sensing surface using 10 mM phosphate buffered saline (pH 7.4) [30]. Washing steps were performed between each surface modification with 10 reaction volume of the above buffer. Analytical grade absolute ethanol (99.9 %) and acetone (99.5 %) were purchased from DKSH, Malaysia. The surface morphology at nanoscale level was measured through field emission scanning electron microscopy (FESEM, Hitachi, S-4300 SE, Japan) and field emission transmission electron microscopy (FETEM, F20-Tecnai, Columbus).

2.2. Fabricating the sensing electrode

The interdigitated electrode (IDE) was fabricated using a wet-etching method. In the initial step, the desired pattern was outlined and further modified [31]. The resulting device measured 12 μm in length and 6 μm in width, featuring 16 fingers arranged in a parallel pattern. The gap and finger regions measured 250 μm, and they were situated in the active electrode region on the sensing surface with a 6 μm square. The electrode surface preparation involved the following procedures: (i) The silicon wafer substrate was transformed into silicon dioxide (SiO_2) through a thermal oxidation process at 500 °C. (ii) A layer of aluminum was deposited using a thermal evaporator. (iii) A positive photoresist with a thickness of 2000 nm was applied to the SiO_2-aluminum (Al) layer using a spin-coater. (iv) The pattern was created on the SiO_2–Al-photoresist surface through exposure to Ultraviolet light for 10 s. (v) The uncovered surface was cleared by immersing the electrode in a developing solution, followed by a 1-min hard-baking process at 110 °C. (vi) Finally, the IDE underwent immersion in an Aluminum-etching solution, followed by rinsing with deionized water and acetone. All experiments were conducted on sensing surfaces fabricated from the same batch.

2.3. Antibody immobilization on nanodiamond

The immobilization of the antibody on the IDE was facilitated using nanodiamond [32], which provides additional surface area on the sensor. Initially, the nanodiamond underwent modification with CDI for antibody attachment, as this linker exposes the antigen-binding region. In brief, 10 mg of nanodiamond was suspended in 100 mM CDI and allowed to remain in solution for 2 h. Subsequently, the modified nanodiamond was washed with a solution of 25 % ethanol and distilled water to remove the unbound CDI. The CDI-modified nanodiamond (nanodiamond-CDI) was then collected by centrifugation at 10,000×*g* for 10 min. To attach the antibody to the nanodiamond, a preliminary assessment indicated the use of 250 nM of polyclonal antibody, which was pre-mixed with the nanodiamond-CDI conjugate and allowed to rest for 2 h. The modified nanodiamond was then washed with PBS to eliminate excess antibody, and the nanodiamond-modified antibody (nanodiamond-antibody) was collected by centrifugation at 10,000×*g* for 10 min.

2.4. Seeding nanodiamond-antibody on the sensing electrode surface

The nanodiamond-antibody modification was affixed to the IDE surface through APTES [33], which facilitates the formation of a self-assembled monolayer. The following steps were employed for this process: (i) 1 % potassium hydroxide (KOH) was added to the IDE surface to create a hydroxyl-tethered surface, allowing it to rest for 10 min. Subsequently, any remaining KOH was removed using distilled water. (ii) APTES (1 % diluted in ethanol) was applied to the electrode surface and allowed to sit for 3 h. Unbound APTES was then washed out with 25 % ethanol. (iii) A 5 μL drop of the nanodiamond-antibody complex was placed on the APTES-modified IDE for 1 h, followed by the removal of excess nanodiamond-antibody using PBS. (iv) Polyethylene glycol-COOH (1 mg/mL) was employed to cover any remaining free APTES areas and reduce biofouling. This nanodiamond-antibody-seeded electrode surface was utilized for evaluating RUNX2 interaction and subsequent quantification.

2.5. Sandwich assay for RUNX2 quantification

A sandwich assay utilizing two different anti-RUNX2 antibodies was conducted on the nanodiamond antibody-functionalized surface to quantify the level of RUNX2. Various concentrations of RUNX2 were individually applied to the nanodiamond-antibody surfaces and allowed to incubate for 15 min to facilitate the interaction between RUNX2 and the antibody. Subsequently, unbound RUNX2 was washed out with a volume of 10 mM PBS (pH 7.4), and the current response was recorded within the desired range (0–2 V). Differences in current were calculated to confirm the binding of RUNX2 with its antibody. For the sandwich assay, 250 nM monoclonal antibody was applied to the RUNX2-interacted IDE surface and incubated for 15 min. The current response was recorded after washing with a volume of 10 mM PBS (pH 7.4) to confirm the sandwich assay involving the polyclonal antibody RUNX2-monoclonal antibody (antibody-RUNX2-antibody). To prevent non-specific binding, both polyclonal and monoclonal antibodies were utilized, as they are expected to have different antigen-binding regions. The experiments were performed three times, and the data were represented by averaging. Sensitivity was assessed as a measure of the method's ability to discriminate between minute variations in the concentration of different samples or the response to changes in analyte concentration. The limit of detection (LOD) was determined as the lowest concentration of an analyte (from the calibration line at low concentrations) against the background signal (S/N = 3:1). In other words, LOD = standard deviation of the baseline + 3σ.

2.6. Biofouling and selective experiment on a nanodiamond-modified electrode surface

Biofouling experiments were carried out using nonimmune antibodies and unrelated proteins to assess the specificity of RUNX2 detection. Performances involving (i) nonimmune antibody in place of polyclonal antibody; (ii) Bovine Serum Albumin (BSA) instead of RUNX2; and (iii) Tumor Necrosis Factor-alpha (TNF-α) substituted for RUNX2 were conducted to confirm the specific detection of RUNX2. Selective experiments were performed by spiking different concentrations of RUNX2 in 1:100 diluted human serum, which was then placed on nanodiamond-antibody surfaces and subjected to sandwiching with monoclonal antibody. All other procedures were conducted following the description provided above. To assess reproducibility, three different devices were employed from the same fabrication batch. This ensures that the experimental results can be validated across multiple instances, enhancing the reliability and robustness of the findings.

3. Results and discussion

RUNX2 plays a pivotal role in controlling gene expression and determining the fate of cells. This transcription factor is known for its involvement in various biological processes, including adipogenesis, hematopoiesis, and osteogenesis. Adipogenesis refers to the process where stem cells differentiate into fully developed adipocytes, contributing to the generation of adipose tissue. In the context of adipogenesis, transcription factors from the RUNX family, including RUNX2, are instrumental in coordinating patterns of gene expression. Identifying suitable biomarkers for diseases is crucial for diagnosis and understanding disease progression. The Runt-related transcription factor (RUNX) family, including RUNX2, is recognized for its vital roles in cell differentiation and development [34]. RUNX proteins are implicated in diverse biological processes such as hematopoiesis (blood cell formation), osteogenesis (bone formation), neurogenesis (neuron formation), and carcinogenesis (cancer development) [35,36]. They exert their functions by binding to specific DNA sequences in target genes and regulating their expression. In this research, the biomarker 'RUNX2' was quantified as a means to identify osteogenic differentiation. This was achieved using an antibody-based sandwich assay, a technique that enables the precise measurement and analysis of the RUNX2 biomarker in the context of osteogenic differentiation.

Fig. 1 illustrates the identification of RUNX2 on a nanodiamond-modified interdigitated electrode (IDE) surface. IDE designs, known for their numerous advantages, are widely utilized in various sensors. IDE structures consist of conductive material fingers that interdigitate to form a periodic pattern. This architectural configuration is commonly employed in diverse sensor types, including chemical, biological, and gas sensors. The benefits of IDE designs include a larger surface area, enhanced sensitivity, reduced noise, faster response times, and increased customization options. Due to these advantageous characteristics, IDE sensors find applications across various fields, providing practical and cost-effective solutions for sensing a wide spectrum of analytes. In the current research, the electrode underwent KOH treatment, followed by APTES attachment. Additionally, CDI-coated nanodiamonds were introduced to the surface. Nanodiamonds, typically in the nanometer range, possess unique qualities that make them appealing for sensing applications, including biocompatibility, chemical stability, large surface area, and adaptability. These features make nanodiamond-immobilized sensing surfaces attractive for various sensing applications, especially in medical diagnostics. The immobilization process involved the activation of ends on the CDI-nanodiamond with amine on the APTES surface. Subsequently, the capture antibody was attached to this nanodiamond-seeded surface through CDI on the nanodiamond and amine on the antibody. This immobilization strategy enhances antibody binding on the IDE, subsequently increasing the amount of RUNX2 binding on the IDE. Finally, a sandwich assay was performed by introducing a detection antibody, completing the process of identifying RUNX2 on the nanodiamond-modified IDE surface.

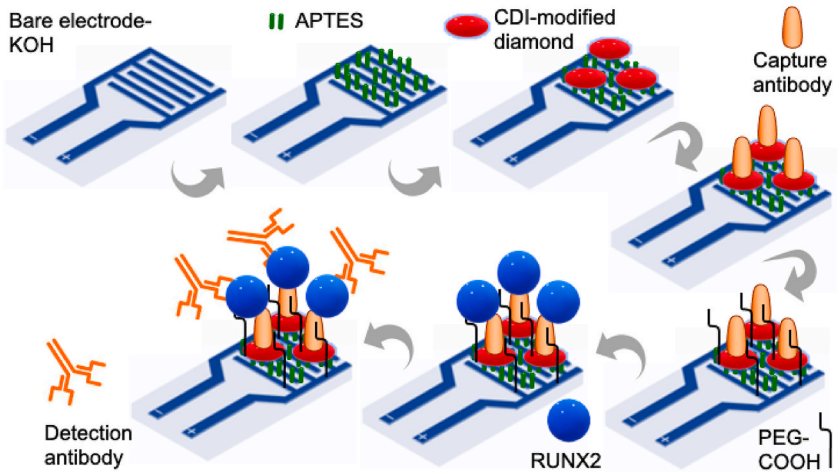

Fig. 1. Schematic illustration of RUNX2 identification on nanodiamond-modified electrode surface. IDE surface was initially treated with KOH and then APTES was attached. Furthermore, CDI-coated nanodiamond was attached and then antibody was immobilized on the nanodiamond through CDI-amine interaction. Finally, the sandwich assay was conducted by introducing a detection antibody.

3.1. Surface characterization of nanodiamond

The surface of the modified nanodiamond was examined through FESEM (Field Emission Scanning Electron Microscopy) and FETEM (Field Emission Transmission Electron Microscopy) analyses. In Fig. 2a and b, FESEM images of the nanodiamond are presented with scales of 500 and 200 nm, respectively. These images reveal a spherical shape of the nanodiamond with a uniform distribution, and the size range was determined to be approximately 20 ± 5 nm. Moving to Fig. 2c and d, FETEM images of nanodiamonds are displayed with configurations of 50 and 20 nm, confirming uniform shapes and sizes. The results obtained from FETEM analysis complement the observations from FESEM. Furthermore, FESEM-EDX results provided additional information, confirming the composition of the modified nanodiamond. The analysis confirmed the presence of approximately 94 % carbon and approximately 6 % nitrogen and oxygen in the nanodiamond structure (Fig. 2e). This comprehensive imaging and elemental analysis offer insights into the morphology and composition of the modified nanodiamond, crucial for understanding its properties and suitability for various applications.

3.2. Comparing antibody attachment with and without nanodiamond

The attachment of the capture antibody plays a crucial role in the detection of antigens, and numerous studies have demonstrated that using a higher number of capturing molecules significantly lowers the limit of detection for the target. In this study, an anti-polyclonal antibody was affixed to the IDE electrode surface as the capture molecule for detecting RUNX2. Typically, antibodies are immobilized on the surface using a chemical linker. In this research, CDI-coated nanodiamonds were employed as the linker to immobilize the antibody on the IDE. Specifically, 250 nM of polyclonal antibody was utilized for immobilization on CDI-nanodiamonds. Following washing, it was determined that approximately 70 % of the antibody was successfully attached to the CDI-nanodiamonds. The efficiency of antibody immobilization using both a conventional chemical linker and the nanodiamond-mediated linker was compared by analyzing the changes in current. Microscopic observations revealed no size variation or aggregation upon antibody immobilization on nanodiamonds. Fig. 3 provides a visual comparison of the antibody experiment with and without nanodiamonds. In Fig. 3a, the antibody attachment through the APTES chemical linker is displayed, where the amine group on APTES interacts with the COOH in the antibody. The current response of the KOH-treated bare IDE was measured at 1.6×10^{-11} A. Following APTES modification, the current increased to 7.48×10^{-10} A. This enhancement can be attributed to the hydroxylated surface, which facilitates improved surface modification by APTES. Subsequently, antibody attachment to APTES further increased the current response to 2.67×10^{-9} A, indicating successful binding of the antibody to the amine-modified surface. This change was attributed to the binding of the COOH group in the antibody with the amine group from the APTES-modified surface. Finally, PEG-COOH was introduced to cover the uncovered APTES as a blocking agent, where COOH in the PEG interacts with the excess amine on the APTES-modified surface, registering a current response of 6.27×10^{-9} A. These cumulative current changes confirm the successful attachment of the antibody to the sensing electrode. This attachment process was compared with antibody attachment through the nanodiamond. The bare electrode and APTES modification displayed current levels of 1.6×10^{-11} and 7.48×10^{-10} A, respectively. Upon CDI-nanodiamond attachment, the current increased to 1.25×10^{-9} A (Fig. 3b). Furthermore, upon adding the

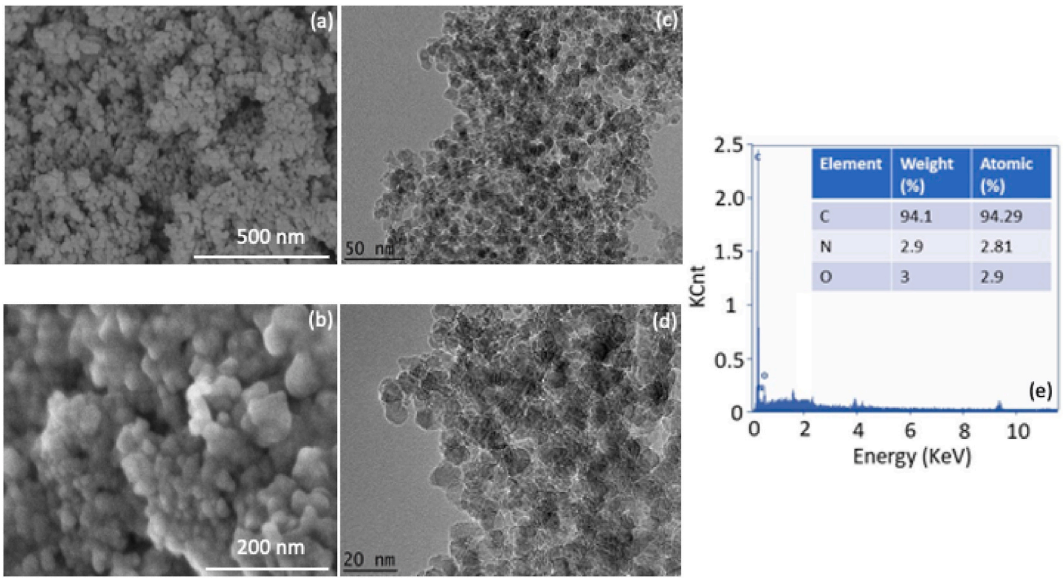

Fig. 2. Imaging of nanodiamond with FESEM and FETEM observation. (a) FESEM with 500 nm; (b) FESEM with 200 nm; (c) FETEM with 50 nm; (d) FETEM with 20 nm. The nanodiamond had a spherical shape with uniform distribution and the size range was identified as approximately 20 ± 5 nm; (e) EDX confirmed the presence of ~94 % carbon and ~6 % of nitrogen and oxygen.

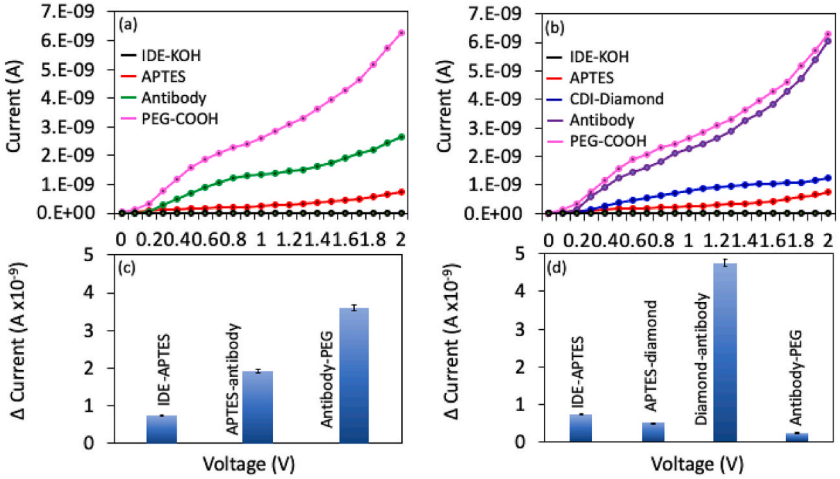

Fig. 3. Comparison experiment of antibody with and without nanodiamond. (a) without nanodiamond; (b) with nanodiamond; (c) Current difference of antibody attachment without nanodiamond; (d) Current difference of antibody attachment with nanodiamond. Antibody attachment with nanodiamond shows a higher current response. Data were averaged by triplicate values.

antibody, the current significantly increased due to the higher number of antibodies attaching to the nanodiamond. Subsequent addition of PEG-COOH resulted in a slight variation in the current response. When comparing the two methods of antibody attachment, the current response was higher with nanodiamond. The differences in current for antibody attachment with and without nanodiamond were 1.92 and 4.75 $\times$ 10^{-9} A, respectively (Fig. 3c and d). This indicates more than two rounds of antibody immobilization on the nanodiamond-modified surface, as the higher number of antibodies can attach to the surface of a single nanodiamond due to the increased presence of CDI.

3.3. *Detection of RUNX2 by capture antibody*

The determination of RUNX2 was conducted using the immobilized capture antibody, as described in section 2.5 of the methodology. Prior to that, the current response of the antibody-attached surface was recorded. Subsequently, various concentrations (0.1, 1, 10, 100, 1000, 2000, 3000 ng/mL) of RUNX2 were added to the antibody-attached surfaces, and the current was recorded again. As illustrated in Fig. 4a, the PEG–COOH–modified electrode displayed a current of 6.27 $\times$ 10^{-9} A. Upon introducing RUNX2, the current began to increase with the rising concentration of RUNX2. At lower levels of RUNX2, minimal interaction occurred between RUNX2 and antibodies, resulting in a smaller change in current response. However, the use of nanodiamonds for surface functionalization facilitates a more organized arrangement of antibodies, enhancing the capture of even smaller quantities of RUNX2 and leading to an increased current response. Additionally, it was observed that as the concentration of RUNX2 increased, the current response also gradually enhanced. It was noted that in 2000 and 3000 ng/mL, the current responses showed saturated levels. This saturation could be attributed to the potential saturation of RUNX2 interaction with antibodies at 2000 ng/mL. As the level of RUNX2 continues to increase, there may not be enough available interactive antibodies on the sensing surface beyond this concentration, leading to a

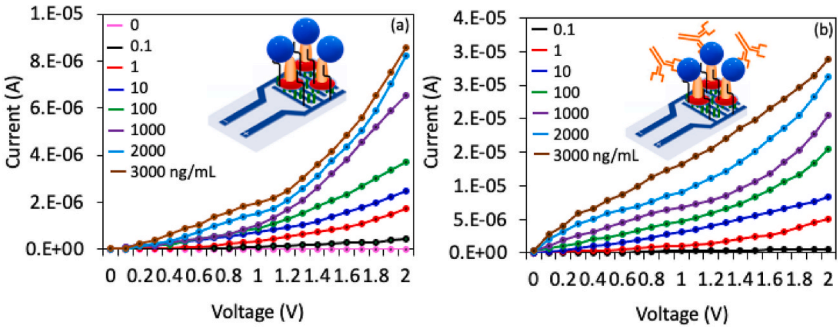

Fig. 4. (a) Detection of RUNX2 on capture antibody immobilized surface. Various concentrations of RUNX 2 were dropped on antibody attached surfaces and the currents were recorded. Furthermore, with increasing concentrations of RUNX 2, the current levels were increased. Figure inset represents the diagrammatic scheme. (b) Sandwich assay of antibody-RUNX2-antibody. A constant concentration of detection monoclonal antibody was dropped on capture antibody-RUNX2 immobilized electrode surfaces. With increasing concentrations of RUNX 2, the current levels were increased. The figure inset represents the diagrammatic scheme.

plateau in the signal response.

3.4. Sandwich assay for RUNX2 identification

For the sandwich assay of antibody-RUNX2-antibody, a constant concentration of the detection monoclonal antibody was applied to the capture antibody-RUNX2 immobilized electrode surface. In Fig. 4b, the current response of the detection antibody binding for different concentrations of RUNX2 is depicted. As the detection antibody was introduced to the IDE surface with attached RUNX2, a sandwich formation occurred, resulting in an increased current response depending on the concentration of RUNX2. Higher concentrations of RUNX2 exhibited a more pronounced difference in current responses, attributed to the larger number of RUNX2 molecules on the surfaces, allowing for greater interaction with antibodies and thereby enhancing the current responses. It was observed that with increasing RUNX2 concentrations, current responses also gradually enhanced. Furthermore, in 2000 and 3000 ng/mL, RUNX2 showed saturation of the current response. As shown in Fig. 5a, the current response was much higher with the capture antibody-RUNX2-detection antibody interaction than with the capture antibody-RUNX interaction. This higher response aids in identifying RUNX2 with a more significant difference in the current response. Additionally, to calculate the limit of detection of RUNX2, the current difference for each RUNX concentration was calculated and plotted in Excel (Fig. 5b). The detection limit was determined as 0.1 ng/mL with antibody-RUNX-antibody, and it dropped 10-fold in the case of the capture antibody-RUNX, with R2 values of 0.9663 and 0.9914, respectively. At the same time, a much higher current difference was noted with the sandwich assay. This lower-level detection of RUNX2 is crucial for quantifying RUNX2 and monitoring osteogenic differentiation. Similarly, various sensors have been introduced by researchers to monitor other transcription factors. For instance, a single-molecule DNA-based biosensor was developed to identify transcription factors by colocalizing the two halves of the binding sites with the attached single molecules of a two-color DNA-based biosensor, achieving detection as low as 150 pM [37]. In another study, the transcription factor SOX9 was detected using the sticky end biosensor method to monitor transcription factor and DNA binding activity, helping to monitor live cell activity [38]. In our sandwich assay, the transcription factor RUNX2 was successfully detected as low as 0.1 ng/mL, providing valuable insights for monitoring the condition of osteogenic differentiation.

3.5. Biofouling and selective detection on a nanodiamond-modified electrode

Biofouling experiments were conducted with a nonimmune antibody and control proteins. Reducing biofouling is a crucial aspect of biosensors as it can significantly impact the detection limit. Various blocking molecules, including ethanolamine, BSA, and PEG-derivatives, are commonly employed to cover the excess space on the sensing electrode surface. Among these, PEG-polymers have gained widespread attention in the biosensor field due to their inert nature, water solubility, ease of surface functionalization, non-toxicity, and lower cost [39–41]. PEGylated particles have demonstrated resistance to biofouling biomolecules owing to their hydrophilic nature and flexibility [42]. In our surface functionalization, there is a possibility that antibodies could interact with the APTES surface instead of RUNX2, leading to an increase in the signal-to-noise ratio. Therefore, PEG-COOH was utilized to block the excess APTES surface and control the biofouling effect of antibodies on the IDE electrode surface. Four different control experiments were conducted on PEG–COOH–blocked IDE electrode surfaces. As illustrated in Fig. 6a, the use of a nonimmune antibody instead of a polyclonal antibody, BSA instead of RUNX2, and TNF-α instead of RUNX2 did not yield any current responses compared to the specific

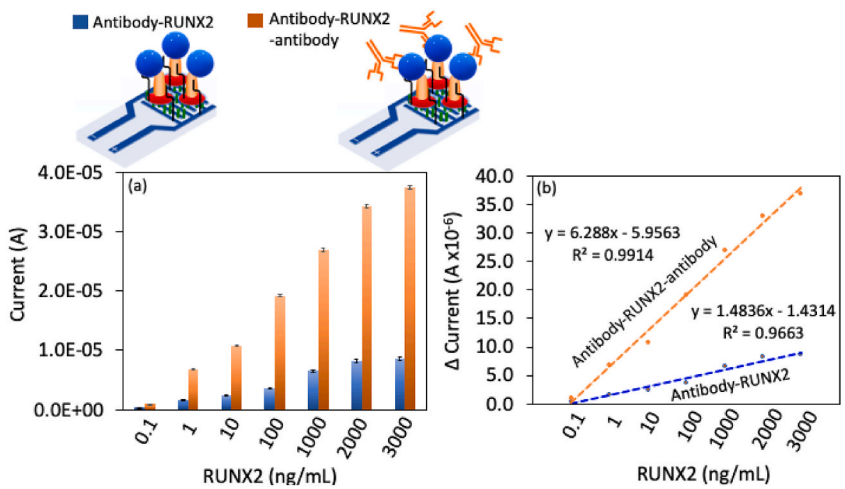

Fig. 5. (a) Comparison of RUNX2 detection with capture antibody-RUNX2 and Capture antibody-RUNX2-detection antibody complexes. The current response was much higher with capture antibody-RUNX2-detection antibody interaction than with capture antibody-RUNX. The figure inset represents the diagrammatic scheme. Data were averaged with triplicate values. (b) The current difference for each RUNX2 concentration was calculated and plotted in an Excel sheet. The detection limit was calculated as 0.1 ng/mL and 1 ng/mL on capture antibody-RUNX and sandwich assay with the R^2 values of 0.9663 and 0.9914, respectively.

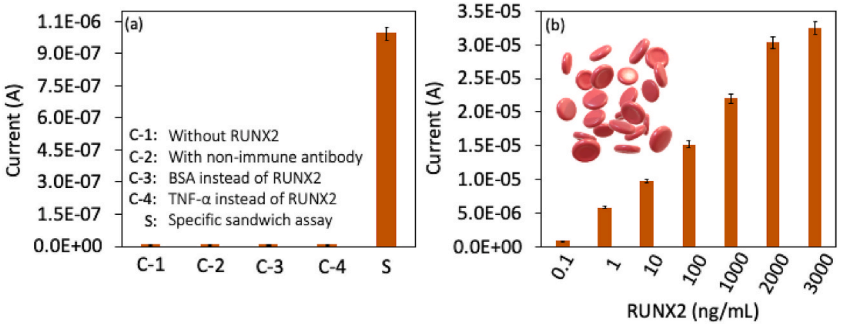

Fig. 6. (a) Biofouling experiments with nonimmune antibody and control proteins. Control experiments did not show any current response compared with specific molecule, confirming the specific detection of RUNX2. (b) Selective experiments were performed by using RUNX2-spiked human serum. All the concentrations of RUNX2-spiked serum were recognized by anti-RUNX2 antibody, indicating the selective detection of RUNX2 by sandwich pattern. Data were averaged by triplicate values.

experiment, confirming the specific detection of RUNX2.

Selective experiments were conducted using RUNX2-spiked human serum. Different concentrations of RUNX2 were spiked in 1:100 diluted human serum and applied to nanodiamond-antibody surfaces instead of RUNX2, and the current response was recorded. As depicted in Fig. 6b, all concentrations of RUNX2-spiked serum were detected by the anti-RUNX2 antibody, indicating the selective detection of RUNX2 through the sandwich pattern. The conditions required for any stem cell do not significantly change among research methods; however, various approaches are employed to assess the level of differentiation. Reverse transcriptase PCR (RT-PCR) is used for detecting osteogenic transcripts, enzyme-linked immunosorbent assay (ELISA) for secreted protein markers, colorimetric tests for osteogenic enzymes, and direct labeling of matrix components. RUNX2, being a transcription factor crucial for osteoblast differentiation and maturation, as well as bone formation and development, is an essential marker. Therefore, assessing RUNX2 aids in determining the osteogenic differentiation of various stem cells, such as bone marrow mesenchymal stroma cells (BMSC) and ADSC [40]. RUNX2 serves as a common marker for osteogenic differentiation in these cells, making the present method suitable for determining RUNX2 in stem cells. Studying this biomarker has revealed various promising therapeutic applications, including the treatment of bone deformities, cartilage injuries, and other disorders requiring tissue regeneration. Researchers continue to investigate these stem cells to better understand their characteristics and clinical utility.

4. Conclusion and future perspectives

Adipose-derived stem cells (ADSCs) have garnered significant attention in the field of bone tissue engineering and regeneration. Monitoring osteogenic differentiation is crucial for understanding directional differentiation and unraveling the developmental mechanisms for applications in tissue engineering. Runt-related transcription factor (RUNX2) plays a crucial role in the early stages of cell differentiation and quantifying its level aids in monitoring osteogenic differentiation. In this experiment, a high affinity impedimetric sandwich biosensor was developed to quantify RUNX2. A nanodiamond-modified interdigitated electrode (IDE) was employed for the antibody-antibody sandwich assay to quantify RUNX2. A higher number of capture antibodies were achieved on the diamond-modified IDE through the amine linker, followed by a sandwich assay using the detection antibody. This assay on the diamond-modified IDE detected RUNX2 at concentrations as low as 0.1 ng/mL. Biofouling experiments with TNF-α, BSA, and nonimmune antibody did not elicit an increase in current, indicating the specific detection of RUNX2. Furthermore, RUNX2-spiked human serum demonstrated an increment in the current response at all RUNX2 concentrations without interference, confirming the selective detection of RUNX2. This sensing system can potentially be extended to test other targets and may be applicable for multiplex testing. Additionally, the RUNX biosensing system can be tested in real biological samples to quantify RUNX2 and monitor osteogenic differentiation. Other transcription factors, such as ZNF25, SOX9, and osterix, can be monitored using suitable probe molecules. While the current optimization with the target (RUNX2) is suitable for clinical practices, testing other clinical biomarkers may require fine-tuning on the sensing surface through further optimization. Practical application necessitates testing the sensing platform with clinical specimens through multiple-phase trials.

Data availability

No data has been used from the public data base.

Funding

None.

CRediT authorship contribution statement

Qingshan Sun: Writing – review & editing, Writing – original draft, Validation, Methodology, Investigation, Formal analysis, Data curation, Conceptualization. **Wei Zhu:** Writing – review & editing, Writing – original draft, Validation, Methodology, Investigation, Formal analysis, Data curation, Conceptualization. **Endong Shi:** Writing – review & editing, Visualization, Validation, Formal analysis, Data curation. **Maheng Bai:** Writing – review & editing, Visualization, Validation, Formal analysis. **Zengliang Liu:** Writing – review & editing, Visualization, Validation. **Zhiquan Yang:** Writing – review & editing, Visualization, Validation, Supervision, Resources, Project administration, Investigation, Conceptualization.

Declaration of competing interest

The authors declare that they have no known competing financial interests or personal relationships that could have appeared to influence the work reported in this paper.

References

[1] J. Zhang, Y. Rong, C. Luo, W. Cui, Bone marrow mesenchymal stem cell-derived exosomal LINC00847 inhibits the proliferation, migration, and invasion of Ewing sarcoma, J Clin Transl Res (2022) 25138–25152, https://doi.org/10.18053/jctres.08.202206.015.

[2] Carolina, Raquel Garcia Latorre, Alberto Martinez-Lorca, Eva Fernazdez, Raul Hernanz, Mercedes Martin, Jose A. Dominguez, Teresa Munoz, Elena Canales, Carmen Vallejo, Marina Alarza, Asuncion Hervas, Manuel Garvi, Vanesa Pino, Sansoles Sancho, Interobserver variability in GTV contouring in non-spine bone metastases, J Clin Transl Res 8 (2022) 465–469, https://doi.org/10.18053/jctres.08.202206.003.

[3] R. Marsell, T.A. Einhorn, The biology of fracture healing, Injury 42 (2011) 551–555, https://doi.org/10.1016/j.injury.2011.03.031.

[4] M. Farrugia, B. Baron, The role of TNF-α in rheumatoid arthritis: a focus on regulatory T cells, J Clin Transl Res 2 (2016) 84–90, https://doi.org/10.18053/jctres.02.201603.005.

[5] D. Holmes, Non-union bone fracture: a quicker fix, Nature 550 (2017) S193, https://doi.org/10.1038/550S193a.

[6] H. Jung Jo, M. Sung Kang, H. Jeong Jang, I. Selestin Raja, D. Lim, B. Kim, D.-W. Han, Advanced approaches with combination of 2D nanomaterials and 3D printing for exquisite neural tissue engineering Materials Science in, Addit. Manuf. 2 (2023) 620, https://doi.org/10.36922/msam.0620.

[7] S. Ahmadi, M. Dadashpour, A. Abri, N. Zarghami, Long-term proliferation and delayed senescence of bone marrow-derived human mesenchymal stem cells on metformin co-embedded HA/Gel electrospun composite nanofibers, J. Drug Deliv. Sci. Technol. 80 (2023) 104071, https://doi.org/10.1016/j.jddst.2022.104071.

[8] M. Dadashpour, H. Mahmoudi, Z. Rahimi, R. Janghorbanian Poodeh, H. Mousazadeh, A. Firouzi-Amandi, Y. Yazdani, A. Nezami Asl, A. Akbarzadeh, Sustained in vitro delivery of metformin-loaded mesoporous silica nanoparticles for delayed senescence and stemness preservation of adipose-derived stem cells, J. Drug Deliv. Sci. Technol. 87 (2023) 104769, https://doi.org/10.1016/j.jddst.2023.104769.

[9] F. Paduano, M. Marrelli, M. Amantea, C. Rengo, S. Rengo, M. Goldberg, G. Spagnuolo, M. Tatullo, Adipose tissue as a strategic source of mesenchymal stem cells in bone regeneration: a topical review on the most promising craniomaxillofacial applications, Int. J. Mol. Sci. 18 (2017) 2140, https://doi.org/10.3390/ijms18102140.

[10] Z.L. Deng, K.A. Sharff, N. Tang, W.X. Song, J. Luo, X. Luo, J. Chen, E. Bennett, R. Reid, D. Manning, A. Xue, A.G. Montag, H.H. Luu, R.C. Haydon, T.C. He, Regulation of osteogenic differentiation during skeletal development, Front. Biosci. 13 (2008) 2001–2021, https://doi.org/10.2741/2819.

[11] M. Mofarrah, D. Jafari-Gharabaghlou, M. Dadashpour, N. Zarghami, Fabricating ZSM-5 zeolite/polycaprolactone nano-fibers co-loaded with dexamethasone and ascorbic acid: potential application in osteogenic differentiation of human adipose-derived stem cells, J. Drug Deliv. Sci. Technol. 79 (2023) 103999, https://doi.org/10.1016/j.jddst.2022.103999.

[12] R. Shinde, I. Juwarwala, V. Modi, C.V. Chandarana, Utility of cardiac biomarkers and biosensors for diagnosis of acute myocardial infarction, Global Translational Medicine 2 (2023) 403, https://doi.org/10.36922/gtm.0403.

[13] Y. Chen, W. Zhou, Y. Gong, X. Ou, A N6-methyladenosine-related long noncoding RNA is a potential biomarker for predicting pancreatic cancer prognosis, Tumor Discovery 1 (2022) 165, https://doi.org/10.36922/td.v1i2.165.

[14] Q. Yu, Y. Jiao, R. Huo, H. Xu, J. Wang, S. Zhao, Q. He, J. Zhang, Y. Sun, S. Wang, J. Zhao, Y. Cao, Application of the concept of neural networks surgery in cerebrovascular disease treatment, Brain & Heart 1 (2022) 223, https://doi.org/10.36922/bh.v1i1.223.

[15] J. Steinman, A. Ovcjak, Z. Luo, X. Zhang, L.R. Britto, J.T. Henderson, H.-S. Sun, Z.-P. Feng, Transient receptor potential melastatin 2 channels in neurological disorders: mechanisms and animal models, Advanced Neurology 1 (2022) 1–18, https://doi.org/10.36922/an.v1i1.3.

[16] H. Chen, N. Du, L. Wang, L. Yang, A higher risk for melanoma in patients with Parkinson's disease: based on the results from National Health and Nutrition Examination Survey 2001 – 2004, Journal of Clinical and Basic Psychosomatics 1 (2023) 0571, https://doi.org/10.36922/jcbp.0571.

[17] H. Li, C. Xu, X. Lu, A case report of refractory pulmonary adenocarcinoma, Advances in Radiotherapy & Nuclear Medicine 1 (2023) 883, https://doi.org/10.36922/arnm.0883.

[18] X. Chen, S. Liu, Z. Zhang, Y. Zhang, Gene-modified T cell therapy for cancer: current challenges and potential solutions, Gene & Protein in Disease 1 (2022) 1–14, https://doi.org/10.36922/gpd.v1i1.114.

[19] Y.-L. Ge, P.-Z. Wang, J.-H. Yan, W. Li, J.-R. Zhang, H. Jin, Y.-P. Yang, F. Wang, D. Li, J. Chen, K. Li, C.-J. Mao, C.-F. Liu, Associations of common variants in TAAR5, OR6C70, and GBA with hyposmia in Han Chinese individuals with Parkinson's disease, Advanced Neurology 1 (2022) 1–6, https://doi.org/10.36922/an.v1i2.71.

[20] L. Zhang, S. Lei, Y. Hu, S. Zhao, M. Zhang, C. Duan, M. Wei, F. Guo, Distinctive clinicopathological features and differential gene expression of cerebral venous thrombosis mimicking brain tumors, Brain & Heart 1 (2023) 188, https://doi.org/10.36922/bh.v1i1.188.

[21] M. Iversen, M. Monisha, S. Agarwala, Flexible, wearable and fully-printed smart patch for pH and hydration sensing in wounds, Int J Bioprint 8 (2022) 41–49, https://doi.org/10.18063/IJB.V8I1.447.

[22] H. Geng, S.C.B. Gopinath, W. Niu, Highly sensitive hepatitis B virus identification by antibody-aptamer sandwich enzyme-linked immunosorbent assay, INNOSC Theranostics and Pharmacological Sciences 5 (2023) 7–14, https://doi.org/10.36922/itps.298.

[23] C.T. Pan, K. Dutt, A. Kumar, R. Kumar, C.H. Chuang, Y.T. Lo, Z.H. Wen, C.S. Wang, S.W. Kuo, PVDF/AgNP/MXene composites-based near-field electrospun fiber with enhanced piezoelectric performance for self-powered wearable sensors, Int J Bioprint 9 (2022) 336–353, https://doi.org/10.18063/IJB.V9I1.647.

[24] P. Sarvari, P. Sarvari, Advances in nanoparticle-based drug delivery in cancer treatment, Global Translational Medicine 2 (2023) 394, https://doi.org/10.36922/gtm.0394.

[25] W. Yu, Z. Xiao, X. Zhang, Y. Sun, P. Xue, S. Tan, Y. Wu, H. Zheng, Processing and characterization of crack-free 7075 aluminum alloys with elemental Zr modification by laser powder bed fusion, Materials Science in Additive Manufacturing 1 (2022) 4, https://doi.org/10.18063/msam.v1i1.4.

[26] M. Heidari Majd, Dual-targeting and specific delivery of tamoxifen to cancer cells by modified magnetic nanoparticles using hyaluronic acid and folic acid, Tumor Discovery 1 (2022) 1–9, https://doi.org/10.36922/td.v1i1.41.

[27] M.S. Yusoff, S.C.B. Gopinath, M.N.A. Uda, T. Lakshmipriya, A.R. Wan Yaakub, P. Anbu, Conjugation of silver and gold nanoparticles for enhancing antimicrobial activity, INNOSC Theranostics and Pharmacological Sciences 4 (2022) 38–47, https://doi.org/10.36922/itps.v4i2.70.

[28] W. Yang, O. Auciello, J.E. Butler, W. Cai, J.A. Carlisle, J. Gerbi, D.M. Gruen, T. Knickerbocker, T.L. Lasseter, J.N. Russell, L.M. Smith, R.J. Hamers, DNA-modified nanocrystalline diamond thin-films as stable, biologically active substrates, Nat. Mater. 1 (2002) 253–257, https://doi.org/10.1038/nmat779.
[29] C.A. Martínez-Huitle, N. Suely Fernandes, S. Ferro, A. De Battisti, M.A. Quiroz, Fabrication and application of Nafion®-modified boron-doped diamond electrode as sensor for detecting caffeine, Diam. Relat. Mater. 19 (2010) 1188–1193, https://doi.org/10.1016/j.diamond.2010.05.004.
[30] Y. Wang, X. Sun, S.C.B. Gopinath, M.S.M. Saheed, X. Wang, Thyroglobulin determination on silane–antibody functionalized interdigitated dielectrode surface to diagnose thyroid tumor, Biotechnol. Appl. Biochem. 69 (2022) 376–382, https://doi.org/10.1002/bab.2116.
[31] S. Ramanathan, S.C.B. Gopinath, Z.H. Ismail, M.K. Md Arshad, P. Poopalan, Aptasensing nucleocapsid protein on nanodiamond assembled gold interdigitated electrodes for impedimetric SARS-CoV-2 infectious disease assessment, Biosens. Bioelectron. 197 (2022) 113735, https://doi.org/10.1016/j.bios.2021.113735.
[32] S.S. Santheraleka Ramanathan, Subash C.B. Gopinath, Zool Hilmi Ismail, No Title Nanodiamond conjugated SARS-CoV-2 spike protein: electrochemical impedance immunosensing on a gold microelectrode, Microchim. Acta 189 (2022) 226.
[33] Z. Yu, S.C.B. Gopinath, T. Lakshmipriya, P. Anbu, Single-walled carbon nanotube-gold urchin nanohybrid for identifying gastric cancer on dimicroelectrodes junction, J. Taiwan Inst. Chem. Eng. 121 (2021) 108–114, https://doi.org/10.1016/j.jtice.2021.04.016.
[34] H. Hojo, S. Ohba, Runt-related transcription factors and gene regulatory mechanisms in skeletal development and diseases, Curr. Osteoporos. Rep. 21 (2023) 485–492, https://doi.org/10.1007/s11914-023-00808-4.
[35] S. Shahriar, Z.T. Rafa, M.S. Mahmood, D. Mahasin, Y. Araf, MdA. Ullah, M.D.H. Rahman, MdA. Ali, F.T. Zohora, C. Zheng, Mohammad Jakir Hosen, Insights into the role of RUNX1 gene in female-related cancers, Gene & Protein in Disease 1 (2022) 147, https://doi.org/10.36922/gpd.v1i2.147.
[36] H. Hojo, Emerging RUNX2-mediated gene regulatory mechanisms consisting of multi-layered regulatory networks in skeletal development, Int. J. Mol. Sci. 24 (2023) 2979, https://doi.org/10.3390/ijms24032979.
[37] K.S. Grußmayer, T. Ehrhard, K. Lymperopoulos, D.P. Herten, Precise quantification of transcription factors in a surface-based single-molecule assay, Biophys. Chem. 184 (2013) 1–7, https://doi.org/10.1016/j.bpc.2013.07.015.
[38] J.P.P. Mendes, N. Zhu, P.K. Wong, A sticky-end probe biosensor for homogeneous detection of transcription factor binding activity, SLAS Technol 28 (2023) 345–350, https://doi.org/10.1016/j.slast.2023.05.001.
[39] T. Lakshmipriya, M. Fujimaki, S.C.B. Gopinath, K. Awazu, Y. Horiguchi, Y. Nagasaki, A high-performance waveguide-mode biosensor for detection of factor IX using PEG-based blocking agents to suppress non-specific binding and improve sensitivity, Analyst 138 (2013) 2863, https://doi.org/10.1039/c3an00298e.
[40] N.Z. Jin, S. Anniebell, S.C.B. Gopinath, Y. Chen, Variations in spontaneous assembly and disassembly of molecules on unmodified gold nanoparticles, Nanoscale Res. Lett. 11 (2016) 399, https://doi.org/10.1186/s11671-016-1615-2.
[41] Y. Nagasaki, Construction of a densely poly(ethylene glycol)-chain-tethered surface and its performance, Polym. J. 43 (2011) 949–958, https://doi.org/10.1038/pj.2011.93.
[42] Y. Nagasaki, Construction of a densely poly(ethylene glycol)-chain-tethered surface and its performance, Polym. J. 43 (2011) 949–958, https://doi.org/10.1038/pj.2011.93.